Orbit Determination and Time Synchronization for the Future Mars Relay and Navigation Constellation

Keidai Iiyama
Aeronautics and Astronautics
Stanford University
William F. Durand Building
496 Lomita Mall
Stanford, CA 94305
kiiyama@stanford.edu

William W. Jun
Jet Propulsion Laboratory
California Institute of Technology
4800 Oak Grove Dr.
Pasadena, CA 91109
william.w.jun@jpl.nasa.gov

Sriramya Bhamidipati
Jet Propulsion Laboratory
California Institute of Technology
4800 Oak Grove Dr.
Pasadena, CA 91109
sriramya.bhamidipati@jpl.nasa.gov

Grace Gao
Aeronautics and Astronautics
Stanford University
William F. Durand Building
496 Lomita Mall
Stanford, CA 94305
gracegao@stanford.edu

Kar-Ming Cheung
Jet Propulsion Laboratory
California Institute of Technology
4800 Oak Grove Dr.
Pasadena, CA 91109
kar-ming.cheung@jpl.nasa.gov

***Abstract*— To enable future human exploration on Mars, it is necessary to develop a dedicated network of satellites that provide both communication relay and positioning, navigation, and timing (PNT) service in Mars' orbit and on its surface. Additionally, it is desirable to operate the constellation semi-autonomously and reduce reliance on the oversubscribed Deep Space Network. In this work, we first address the design of the next-generation Mars constellation with a focus on the following three objectives: coverage between ±30° latitude, communication data volume, and surface user PNT performance. By analyzing the trade-off space, we propose a notional constellation comprising five satellites: two orbiters at areostationary orbit and three orbiters in an inclined ½ repeating ground track orbit, which balances the three objectives effectively. Second, we propose a semi-autonomous orbit determination and time synchronization (ODTS) framework for the MRN orbiters. Our proposed approach fuses range, range-rate, and time difference measurements from inter-satellite links (ISLs) and links with a Mars surface station (MSS), in a centralized batch filter. While eliminating the need for frequent DSN tracking, we demonstrate an improved orbit determination accuracy of up to meter level and timing accuracy of sub-nanosecond level by using a single MSS as an anchor node.**

TABLE OF CONTENTS

1. INTRODUCTION

The current Mars relay network (MRN), which utilizes the combination of NASA and ESA orbiters to transfer data from Mars surface assets, has greatly contributed to the success of past scientific missions [1,2]. However, these orbiters are now operating beyond primary design lifetimes, and were not principally designed for relay services. To enable future human exploration on Mars, it is necessary to develop a dedicated satellite network that provides both communication relay and positioning, navigation, and timing (PNT) service in Mars' orbit and on its surface. Additionally, it is desirable to operate the constellation semi-autonomously and reduce reliance on the oversubscribed Deep Space Network (DSN) [3].

In the paper, we first address the design of the next-generation Mars constellation with a focus on the following three objectives: coverage between $\pm 30^{\circ}$latitude, communication data volume, and surface user PNT performance. Previous studies have addressed various aspects of Mars constellation design. Gladden, et al. (2021) and Long, et al. (2023) investigated various constellations for next-generation Mars telecommunication orbiters and computed available data throughput [4, 5]. Kelly et al. (2018) proposed a Walker-Delta constellation of 15 cubesats to maximize surface coverage [6]. Molli, et al. (2023) proposed a constellation of 5 satellites (1 mothercraft and 4 daughtercrafts) in inclined orbits, which utilizes inter-satellite links (ISLs) for autonomous orbit determination [7]. However, despite these contributions, none have addressed all of the three objectives simultaneously.

To address this gap, our paper conducts a comprehensive analysis of the coverage, communication data volume, and PNT performance for a notional constellation comprising five satellites: two orbiters at areostationary orbits, one orbiter in equatorial repeating ground track (RGT) orbit at a lower altitude than the areostationary orbit, and two orbiters in inclined RGT orbit with the same altitude. By analyzing the trade-offs of orbit altitude and inclination in terms of achieving the three objectives, we propose a candidate constellation that balances the three objectives effectively. There is a trade-off because increasing the inclination enhances the geometrical diversity of the constellation which is beneficial for navigation accuracy but reduces coverage in low latitude regions, while increasing the altitude improves coverage but diminishes data volume from the surface to the orbit.

It is also necessary to achieve precise orbit determination and time synchronization (ODTS) of the MRN orbiters to provide

979-8-3503-5597-0/25/$31.00 ©2025 IEEE

2025 IEEE Aerospace Conference | 979-8-3503-5597-0/25/$31.00 ©2025 IEEE | DOI: 10.1109/AERO63441.2025.11068793

PNT services. Previous studies have analyzed orbit determination accuracy using DSNs [8] and inter-satellite links (ISLs) [7]. However, to the best of the authors' knowledge, there exists no work that analyzes the time synchronization accuracy of the orbiters. In addition, previous works have not considered achieving the data relay and ODTS of the MRN satellites simultaneously.

In this paper, we propose an ODTS framework for the MRN orbiters that achieves orbit determination and time synchronization simultaneously. Our proposed approach integrates two different methodologies: ISLs and links between orbiters and a Mars surface station (MSS). We utilize two-way regenerative links between two orbiters and two-way or one-way links between the MSS and the orbiters to obtain range, range-rate, and differential clock bias measurements. We utilize Gaussian Minimum Shift Keying (GMSK) + pseudo-Noise (PN) ranging links at Ka-band to achieve simultaneous data relay and ranging [9]. The obtained measurements are downlinked to a fusion center, which would likely be a Mars Surface Station, and processed in batches to estimate the orbits and clock biases of the orbiters simultaneously. Within this network connected by ISLs, the surface station serves as anchor nodes since their absolute position and clock offset are known very precisely. Therefore, this approach enables reducing the use of DSN by achieving ODTS within the Mars system.

The contribution of the paper is summarized as follows

- We propose a candidate PNT+communication constellation of 5 satellites in areostationary orbit and repeating ground track orbit, that balances the coverage, surface positioning, and data relay performance.
- We formulate measurement models for two-way ranging and time transfer measurements considering the coupling between orbit and clock bias estimates.
- We propose a batch ODTS framework that combines ISL and links with surface stations on Mars, that is self-contained in Mars, and can reduce reliance on DSN.
- We conduct a Monte-Carlo ODTS simulation for different combinations of links to evaluate the feasibility of the proposed ODTS framework.

The paper is structured as follows. In section 2, we analyze the tradeoff between coverage, navigation, and data relay, and propose a candidate constellation that can balance these three objectives. In section 3, we formulate the two-way range, range-rate, and time-transfer measurements, which consider the coupling between orbit determination and timing. In section 4, we propose a batch processing framework to process the obtained measurements. In section 5, we provide the ODTS results for different combinations of links. Finally, concluding remarks and future works are given in section 6.

2. Constellation Design

We address the design of the next-generation Mars constellation.

Requirements and Design Space

The requirements for the constellation design are as follows

- The ISLs between the two Areostionary orbiters should be continuously available. Similarly, ISLs between two adjacent RGT orbiters should be continuously available. Here, we assume the links are available unless the Martian surface and atmosphere are not blocking the line of sight.
- The three RGT orbiters have continuous coverage of the surface for latitudes between -30° and 30°.
- The crosslinks and the proximity links should be able to achieve data rates over 10 Mbps [10].
- The constellation should be able to provide positioning and timing service for latitudes between -30° and 30°.

We fix the number of satellites for this study. We assume 2 areostationary (AS) orbiters, and 3 orbiters in a repeating ground track (RGT) orbit. One of the RGT orbits is equatorial, and two of them have the inclination of i_{rgt} and $-i_{rgt}$. We assumed the longitude of the ascending node (RANN, Ω) of the 3 orbiters are $0, 120$, and 240.

With these assumptions, the parameters to be explored are the inclination (i_{rgt}) and the altitude (h_{rgt}) of the inner orbiters.

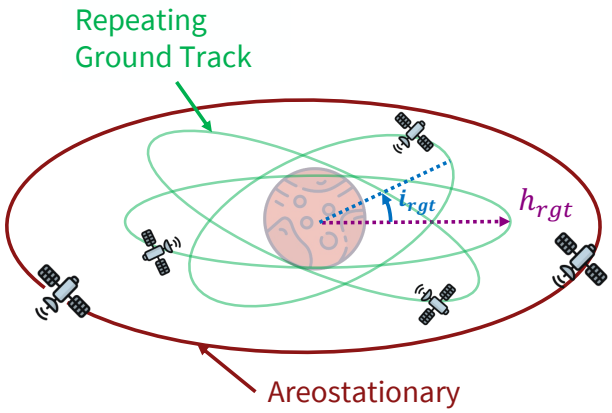

Figure 1: **Search space of the constellation design. We assume a constellation of 2 areostationary (AS) orbiters, and 3 repeating ground track (RGT) orbiters. We search for the inclination i_{rgt} and altitude h_{rgt} that balances surface coverage, navigation accuracy, and data relay volume.**

Inter-satetellite Link Availability

We first look into the ISL availability requirement to constrain the phasing of the areostationary orbiters. The maximum separation $\theta_{sep,max}$ allowed to enable continuous ISLs between the areostationary satellites without being occulted by the Martian atmosphere is

$$\theta_{sep,max} = 2\arccos\left(\frac{R_M + h_{atm}}{R_M + h_{as}}\right) = 160.29^\circ \quad (1)$$

where $R_M = 3396.2$ km is the Mars radius, and $h_{atm} = 100$ km, $h_{as} = 17031.4$ km are the atmosphere mask and the altitude of areostationary satellites. Therefore, we set the separation of the two orbiters to $\theta_{sep,as} = 150^\circ$, allowing a margin of 10.29°.

Analytical Surface Coverage Analysis

Before simulating the surface coverage for different pairs of h_{rgt} and i_{rgt}, we analytically compute the minimum required altitude of the RGT orbiters to constrain the search space.

For the analytical coverage computation, we assume that all three RGT orbiters are equally phased on an equatorial circular orbit with altitude h. The central angle β_0 (as shown

in Figure 2) of the surface coverage circle from a single satellite is given as

$$\beta_0 = \sin^{-1}\left(\frac{d\cos(\epsilon_0)}{a}\right) \tag{2}$$

$$d = R_M\left[\sqrt{\epsilon_0^2 + \left(\frac{R_M+h}{R_M}\right)^2} - 1 - \sin(\epsilon_0)\right] \tag{3}$$

where d is the slant range, and ϵ_0 is the elevation mask. For the three satellites to continuously cover the surface at latitude ϕ, β_0 needs to satisfy the following equation, as shown in Figure 2.

$$\beta_0 \geq \arccos^{-1}\left[\cos(\phi)\cos\left(\frac{\pi}{3}\right)\right] \tag{4}$$

Plugging in the values $R_M = 3396.2, \epsilon_0 = 10°$, we get the minimum required altitude h to have continuous coverage at each latitude. Note that we assume that the antenna on board the orbiters have a large enough swath to cover the surface.

The results are shown in Table 1. To provide coverage up to latitude $\phi = 30°$, we need an altitude of 8995.3 km, which has the orbital period of 11.63 hours (47.25% of Mars sidereal day). Therefore, a 1/2 repeating ground track orbit ($h = 9472$ km) could provide full coverage at latitude $\phi = 30°$.

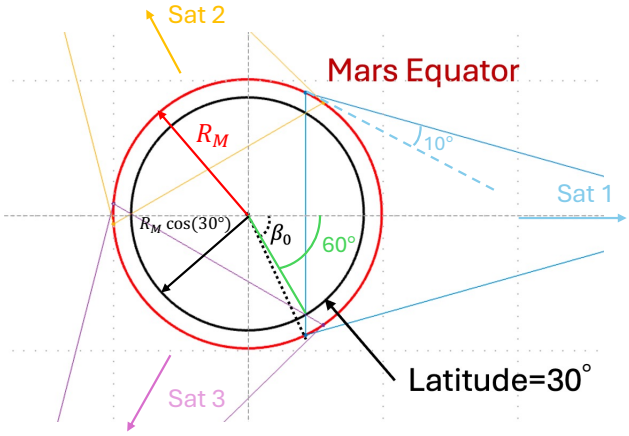

Figure 2: Geometry of the analytical coverage analysis (top view, equatorial plane). In the analytical coverage analysis, we assume that the three satellites are equally phased in the equatorial orbit.

Table 1: Mimimum Altitude for Continuous Coverage with 3 Equatorial Orbiters

Latitude [deg]	Altitude [km]
0	6382.7
10	6624.0
20	7413.0
30	8995.3
40	12031.1
50	18596.81

Coverage Simulation

The analytical minimum altitude computation method cannot be directly applied to inclined orbits. We find the minimum altitude for full coverage for inclined constellations, by evaluating the coverage on discretized time and surface user locations. The simulation parameters for the coverage simulation are summarized in Table 2. The coverage is evaluated as follows

$$(\text{Coverage}) = \frac{\Sigma_{p=1}^{P}\Sigma_{t=1}^{T}V_{pt}}{TP}$$

$$V_{pt} = \begin{cases} 1 & \text{At least one satellite visible at point p at timestep t} \\ 0 & \text{No satellite visible at point p at timestep t} \end{cases} \tag{5}$$

where T, P is the number of timestep and user points, respectively. Note that the surface coverage could only be computed up to a limited accuracy due to discretization errors in time and space.

The coverage simulation result is shown in Figure 3 and Table 3. We observe that the result for the zero inclination case matches with the analytical coverage computation, and the required minimum altitude for full coverage increases as the inclination increases. Note that although the orbit with zero inclination provides the best coverage, introducing inclination increases geometrical diversity. Consequently, adding inclination becomes crucial for enhancing positioning performance in the equatorial region, as we will discuss in the next section. The 1/2 repeating ground track orbit ($h = 9472$ km) with the inclination of 10° can provide over 99% coverage at the latitude $\phi = \pm 30°$.

Note that within the region where the inclination magnitude is below 30°, the latitude band $\phi = \pm 30°$ has the lowest coverage. Therefore, the computed values provides a lower bound for the coverage between $\phi = -30°$ and $\phi = +30°$.

Table 2: Simulation Parameters for the Coverage Simulation

Parameter	Value
Simulation Length	50 orbits
Timestep	1/360 of orbit period
Altitude range [km]	8500 - 15000 (interval: 10)
User point latitude	-30, 30 (2 points)
User point longitude	0, 1, 2, . . . , 359 (360 points)

Table 3: Surface Coverage for Different Orbit Inclinations

Inclination [deg]	Min Altitude for Coverage [km]		
	99%	99.9%	Full
0	8630	8960	9000
5	8820	9830	10230
10	9400	11140	11890
15	10430	12180	14290

Horizontal Dilution of Precision (HDOP) Simulation

When the users on the Martian surface use the navigation signals broadcasted by the satellites, the positioning (and timing) accuracy of the user on the surface is affected by the relative geometry of the navigation satellites with respect

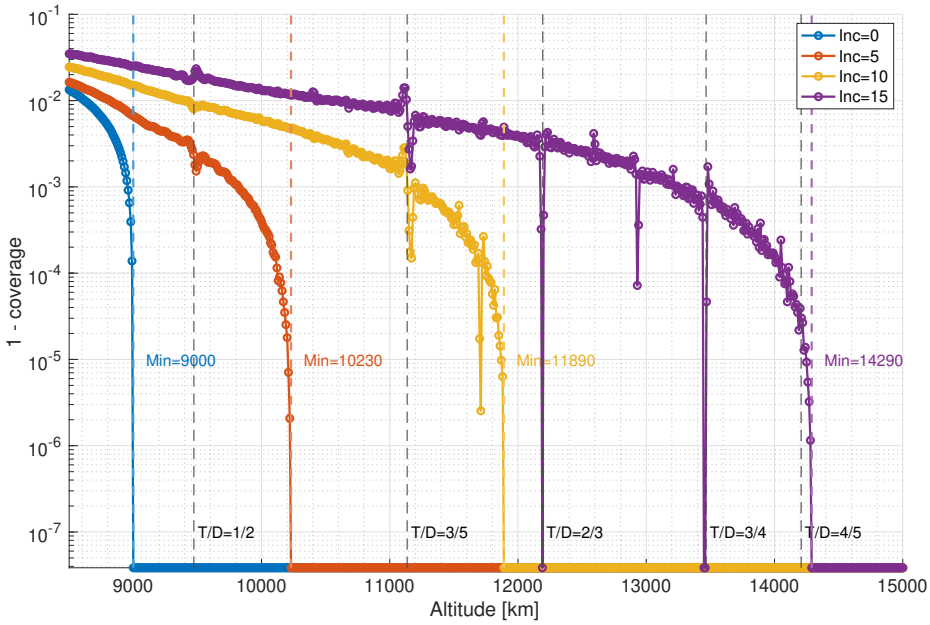

Figure 3: **The simulated coverage at latitude $\phi = \pm 30°$ for different combinations of altitude and inclinations. Note that the y-axis shows 1 - coverage. When the inclination of the two RGT orbiters is set to 0, 5, 10, and 15, the minimum altitude required for full coverage is 9000, 10230, 11890, and 14290 km, respectively. Note that at repeating ground track orbits, the relative geometry repeats every N revolution, which results in the reduction of discretization points and an increase in the coverage metric, which corresponds to the spikes observed in the figure.**

to the user. The measure that shows how favorable the relative geometry is called geometric dilution of precision (GDOP) [11]. GDOP is calculated based on the relative position of 4 or more satellites. However, in our case, the surface user can only see a maximum of three satellites at single epoch, (two RGT satellites and one Areostationary satellite), and therefore the GDOP cannot be calculated. Instead, we computed the horizontal dilution of precision, HDOP, assuming that the vertical position (altitude) and the clock bias of the user can be estimated with other methods. HDOP is computed as follows [12]

$$\text{HDOP} = \text{trace}(G^\top G)^{-1}$$

$$G = \begin{bmatrix} -\frac{e_{s1}}{\sqrt{e_{s1}^2+n_{s2}^2+u_{s1}^2}} & -\frac{n_{s1}}{\sqrt{e_{s1}^2+n_{s2}^2+u_{s1}^2}} \\ \vdots & \vdots \\ -\frac{e_{sm}}{\sqrt{e_{sm}^2+n_{sm}^2+u_{sm}^2}} & -\frac{n_{sm}}{\sqrt{e_{sm}^2+n_{sm}^2+u_{sm}^2}} \end{bmatrix} \in \mathbb{R}^{m\times 2} \tag{6}$$

where e_{si}, n_{si}, u_{si} is the position of satellite $i \in [1, m]$ in East, North, Up (ENU) coordinates centered at the surface user location.

Figure 4 shows how HDOP changes with different RGT orbiter inclinations, for a combination of three 1/2 RGT orbiters and two Areostionary orbiters. The values shown are the median over all longitudes and time epochs. The HDOP of the low latitude regions ($|\phi| < 10°$) is strongly affected by the inclination of the RGT orbiters, because at lower latitude regions the equatorial orbits are clustered near the zenith, and the geometrical diversity of the satellite directions is limited.

Proposed Constellation

Based on the coverage and HDOP analysis, we selected the parameters $i_{rgt} = 10°$ and $h_{rgt} = 9472$ km (1/2 repeating ground track orbit), which shows a good balance between the coverage and navigation objectives: over 99% coverage at $\phi = \pm 30°$, and achieving HDOP < 10 for over 20 % of time near the equator and over 50 % of time at $\phi > 5°$. The orbital elements of the proposed constellation are shown in Table 4, and the orbits of each satellite in a Mars-centered inertial frame are shown in Figure 5.

Table 4: **Orbit elements of the satellites for the proposed constellation. Small eccentricity and inclination are added to avoid singularities.**

Satellite	a [km]	e []	i [deg]	Ω [deg]	w [deg]	M_0 [deg]
RGT 1	12878	0.01	10	0	0	0
RGT 2	12878	0.01	-10	120	0	0
RGT 3	12878	0.01	10^{-3}	240	0	0
AS1	20428	0.01	10^{-3}	0	0	0
AS2	20428	0.01	10^{-3}	0	0	150

Data volume simulation

Finally, we run a link budget analysis to compute the required equivalent isotropic radiated power (EIRP) and transmit power P_{tx} to close the link for different data rates in Mars surface to orbit uplink and ISL for the proposed constellation, and to check if the communication payload sizing is feasible. We assumed the usage of the GMSK + PN scheme, which enables simultaneous data relay and ranging [9]. The equations

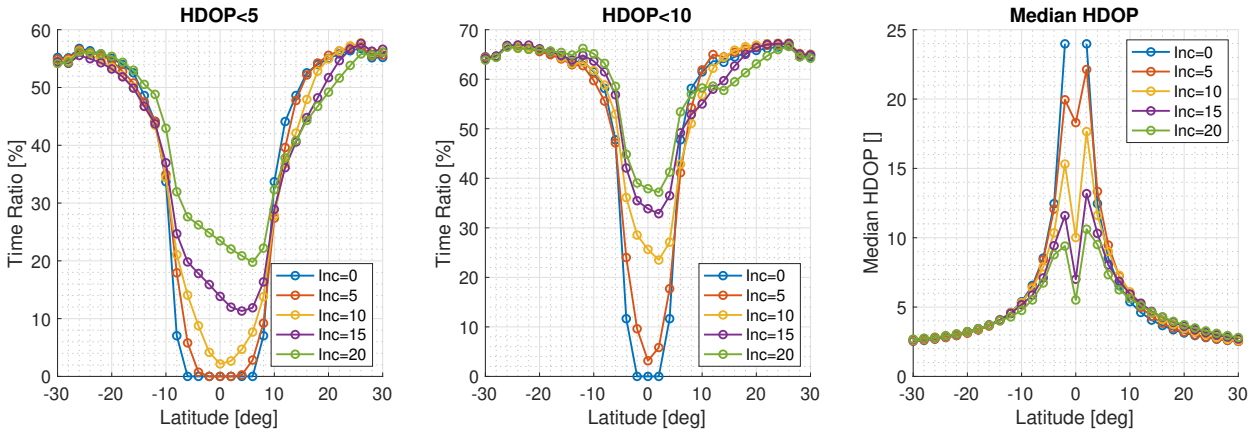

Figure 4: **Time ratios where HDOP is below 5 and 10, and the median HDOP, for different inclinations of the two RGT orbiters. The x-axis is the latitude of the surface user. The values shown are the median over all longitudes. The HDOP of the low latitude regions ($|\phi| < 10°$) improves by increasing the RGT orbit inclination.**

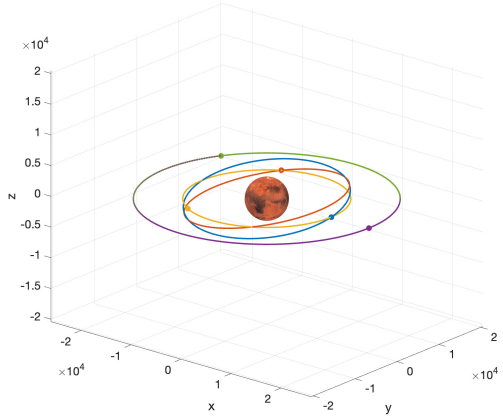

Figure 5: **Proposed Constellation of 5 Orbiters**

used to compute EIRP and P_{tx} from a given data rate D_r are as follows:

$$\text{EIRP}_{dBW} = G_{tx,dB} + P_{tx} \tag{7}$$

$$\left(\frac{P_t}{N_0}\right)_{req,dB} = \text{EIRP}_{dBW} - L_{fs} + 228.6 + \left(\frac{G}{T}\right)_{rx,dB} \tag{8}$$

$$L_{fs} = 20\log_{10}\left(\frac{4\pi D}{\lambda_c}\right) \tag{9}$$

$$\left(\frac{G}{T}\right)_{rx,dB} = G_{rx,dB} - 10\log_{10}(T_{rx}) \tag{10}$$

$$G_{rx,dB} = G_{tx,dB} = 10\log_{10}\left(\eta_{ant}\frac{\pi D_{ant}}{\lambda}\right) - 3\left(\frac{\theta_p D}{70\lambda}\right)^2 \tag{11}$$

$$\left(\frac{P_t}{N_0}\right)_{req,dB} = (SNR)_{req,dB} - 10\log_{10}(T_s) \tag{12}$$

Table 5: **The parameters used for link budget analysis and the ranging noise computation of GMSK + PN links. The values except the Antenna parameters are taken from [13]**

Parameters	Symbols	Value
Frequency (Ka-band)	-	26.5 GHz
GMSK Modulation	BT_s	0.25
Coding rate (concatenated Reed-Solomon & 1/2 convolutional encoder)	r_{code}	1/2.29
PN ranging modulation index	m_{RG}	0.222 rad
PN ranging sequence	-	T4B
Required symbol Error Rate	SER_{req}	0.1
Carrier phase synchronizer bandwidth	$B_L^{carrier}$	50 Hz
Chip phase synchronizer bandwidth (Hz)	B_L^{chip}	5 Hz
E_b/N_0 margin (dB)	$\left(\frac{E_b}{N_0}\right)_{margin}$	3 dB
Antenna Diameter	D_{ant}	40 cm
Antenna Efficiency	η_{ant}	0.5
Antenna Pointing Error	θ_p	5 μrad
Total System Noise Temperature	T_{rx}	470 K

$$(SNR)_{req,dB} = 10\log_{10}(r_{code}) + \left(\frac{E_b}{N_0}\right)_{dB} \tag{13}$$

$$\left(\frac{E_b}{N_0}\right)_{dB} = \left(\frac{E_b}{N_0}\right)_{margin,dB} + \left(\frac{E_b}{N_0}\right)_{req,dB} \tag{14}$$

$$\frac{E_s}{N_0} = L_{tm} \cdot 10^{(SNR)_{req,dB}/10} \tag{15}$$

$$SER_{req} = \frac{1}{2}\text{erfc}\left(\sqrt{\frac{E_s}{N_0}}\right) \tag{16}$$

$$T_s = \frac{D_r}{r_{code}} \tag{17}$$

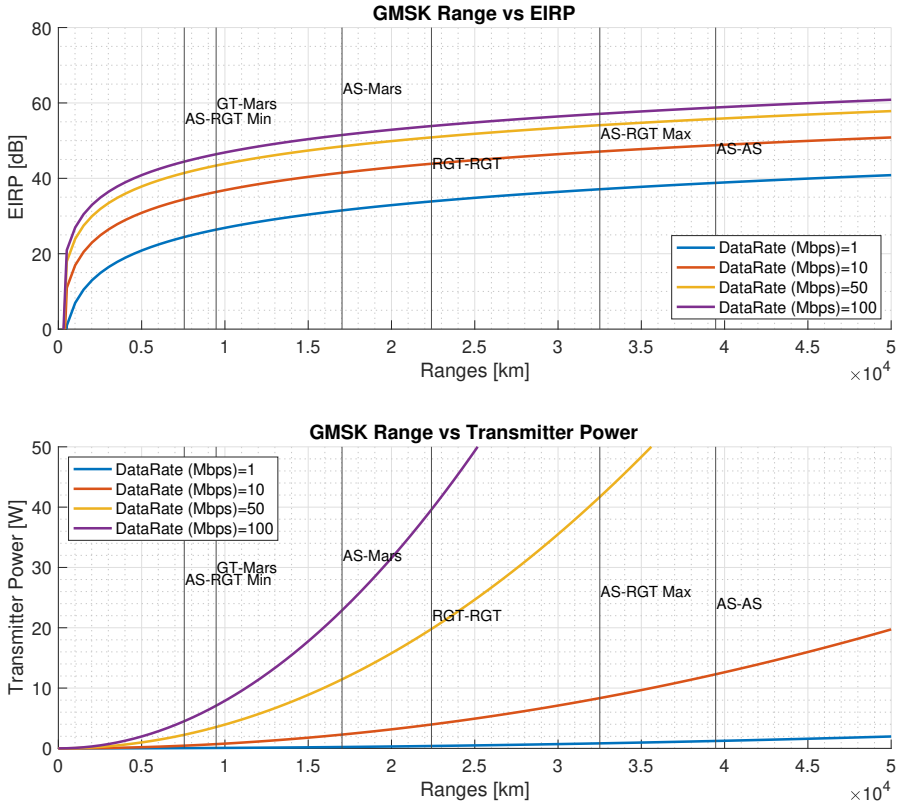

Figure 6: **Required EIRP and transmitter power for different data rates of GMSK + PN links for ISL and surface-to-orbit links. We assumed a $G/T = 10$dB/K for the receiver antenna on the relay satellite for EIRP calculation, and an antenna diameter of 40 cm for the transmission power computation. The other parameters are listed in Table 5.**

where $G_{tx,dB}, G_{rx,dB}$ is the transmitter and receiver gain (dB), P_{tx} is the transmitter power (W), SNR is the signal-to-noise ratio (dB), λ_c is the carrier wavelength, D_r is the datarate (bps), L_{tm} is the telemetry loss (which is a function of SNR), and T_s is the telemetry symbol interval (s) [14]. The notations and the values for other parameters are listed in Table 5.

The results are shown in Figure 6. With the antenna size of 40 cm and 10 W transmission power on Mars surface user, we could achieve $>$ 125 Mbps between surface and RGT orbit, $>$ 50 Mbps between the surface and areostationary orbit. Similarly, with antenna size of 40 cm and 10 W transmission power used for the ISL, we achieve $>$ 50 Mps for the links between RGT orbiters, and $>$ 10 Mbps for the links between areostaionary orbiters. This datarate satisfies all the target data rate in [10] (Tens of Mbps for both ISL and proximity link) .

3. Measurement Models

In this section, we summarize the measurements used for ODTS.

Link Types

We combine the following three types of links.

Inter-satellite links (ISL): This is the link between either two RGT orbiters, RGT orbiter and the AS orbiter, or two AS orbiters.

Mars surface station - RGT orbiter links (MSS-RGT): This is the link between the RGT orbiter and the MSS.

DSN - areostaionary orbiter links (DSN-AS): This is the link between the three DSN stations and the AS orbiter.

The three types of links used are illustrated in Figure 7. For ISL and DSN-AS link, we conduct two-way regenerative coherent ranging to generate measurements for ODTS. For MSS-RGT link, we either conduct two-way regenerative coherent ranging, or one-way ranging.

Two-way Measurements

An overview of two-way time link measurement is illustrated in Figure 8. The link is initiated at the host agent (A), and sent to the target agent (B). In this paper, we call this link an uplink. At B, signals are regenerated, and sent back to the host agent (A). In this paper, we call this link a downlink. The host agent can be a satellite (ISL), MSS, or DSN, and a target agent is one of the satellites in the constellation. The three observable are 1) two-way transfer time τ_{ud}, 2) the local clock time of the reception time for the downlink $\tilde{t}^A_{rx}$, and 3) the local clock time of the reception time for the uplink $\tilde{t}^B_{rx}$. The time-stamp $\tilde{t}^B_{rx}$ is sent to host agent A as part of the

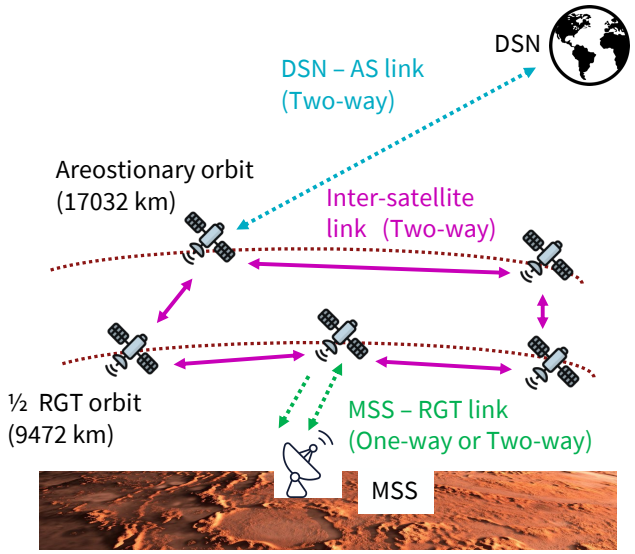

Figure 7: **Illustration of the three types of measurement used in ODTS. For DSN-AS and ISL, we generate two-way links. For MSS-RGT, we generate either two-way or one-way link.**

downlink telemetry.

The three measurements constructed from these observables are 1) two-way range measurement, 2) two-way range-rate measurement, and 3) two-way clock bias measurement. Below, we describe how they are constructed from the observables, as well as their mapping to the estimated states. The overview of the relationship between the states and the measurements is shown in Figure 9.

Two-way range: The two-way range measurement ρ_{ud} is computed as follows

$$\begin{aligned} \rho_{ud} &= \frac{c}{2}\tau_{ud} \\ \tau_{ud} &= \tau_u + \Delta t^B_{rx-tx} + \tau_d + \epsilon_\tau \end{aligned} \tag{18}$$

where τ_{ud} is the measured round-trip time, τ_u, τ_d is the propagation time for the uplink and the downlink, respectively, ϵ_τ is the round-trip time measurement error due to ranging chip jitter, and Δt^B_{rx-tx} is the hardware delay at agent B to coherently regenerate the received signal and transmit it back to agent A. We assume Δt^B_{rx-tx} is known from calibration.

Let $\boldsymbol{r}^A(t) \in \mathbb{R}^3$ and $\boldsymbol{r}^B(t) \in \mathbb{R}^3$ the location of agent A and B at true time t, respectively. Similarly, let $\delta t^A(t)$ and $\delta t^B(t)$ the clock biases of the agents A and B at true time t, respectively. Finally, we represent the local time at agent A, B as $\tilde{t}_A$ and $\tilde{t}_B$, and $\delta t^A(\tilde{t}_A)$ and $\delta t^B(\tilde{t}_A)$ are the clock biases of the agents A and B at their local time, respectively. The local time can be converted to true time (and vice versa) using the relationship below.

$$\tilde{t}_A = t - \delta t_A(t) \approx t - \delta t_A(\tilde{t}_A) \tag{19}$$
$$\tilde{t}_B = t - \delta t_B(t) \approx t - \delta t_B(\tilde{t}_B) \tag{20}$$

The two-way range measurement can also be mapped to the location of the two agents represented in true time as follows

$$c\tau_d = \|\boldsymbol{r}^A(t^A_{rx}) - \boldsymbol{r}^B(t^B_{tx})\| \tag{21}$$
$$t^B_{tx} = t^A_{rx} - \tau_d \tag{22}$$
$$t^B_{rx} = t^B_{tx} - \Delta t^B_{rx-tx} \tag{23}$$
$$c\tau_u = \|\boldsymbol{r}^B(t^B_{rx}) - \boldsymbol{r}^A(t^A_{tx})\| \tag{24}$$
$$t^A_{tx} = t^B_{rx} - \tau_u \tag{25}$$

The downlink light-time delay equations (21) and (22) have to be solved together in an iterative manner, and the same for (24) and (25).

Note that the range measurement is affected by the onboard clock bias estimation error of the agent A (δt^A), because the equation (21) - (25) are represented in true time, and we need the clock bias estimate to compute the (estimated) true time from local time. However, the error introduced by time-tagging becomes small once the clocks are sufficiently well synchronized. For example, if the clock is synchronized in micro second level, since the relative satellite velocities are at maximum in orders of km/s, the ranging error will be in orders of mm.

The measurement error $\epsilon_\rho = (c\epsilon_\tau)/2$ is modeled as a ranging chip jitter variance as follows [13]:

$$\begin{aligned} \epsilon_\rho &\sim \mathcal{N}(0, \sigma^2_\rho) \\ \sigma_\rho &= \frac{T_c c}{2} L_{jitt} \sqrt{\frac{B^{chip}_L T_c}{\pi^2 L_{ck} \frac{P_T T_s}{N_0} 2J^2_1(m_{RG})}} \end{aligned} \tag{26}$$

where $L_{ck} = 0.881$ for code T4B, L_{jitt} is a function of the received SNR $SNR = (P_T T_s)/N_0$ and J_1 is the J_1 Bessel function [15]. We assumed that the chip interval T_c is equivalent to the symbol interval T_s.

Two-way range rate: The two-way range rate measurement $\bar{\dot{\rho}}_{ud}$ is obtained from integrated Doppler count $N_d(t)$, as follows [16]

$$\begin{aligned} \bar{\dot{\rho}}_{ud} &= \frac{c}{2f_{T,0}T_I} n_d + \epsilon_{\dot{\rho}} \\ &= \frac{1}{T_I}\left(\rho_{ud}(t) - \rho_{ud}(t - T_I)\right) + + \epsilon_{\dot{\rho}} \\ N_d(t) &= \int_{t-T_I}^{t} f_T(\tau) - f_R(\tau) d\tau \\ &= n_d + \Delta n_b + \Delta n_y \\ n_d &= f_{T,0}(\tau_{ud}(t) - \tau_{ud}(t - T_I)) \end{aligned} \tag{27}$$

where T_I is the integration time, n_d is the nominal unbiased Doppler count, $f_{T,0}$ is the nominal transmission frequency, and Δn_b and Δn_y are the bias terms from Doppler pre-compensation and transmitter reference frequency noise, respectively. Assuming Δn_b is known, the noise $\epsilon_{\dot{\rho}}$ is modeled as

$$\epsilon_{\dot{\rho}} = \delta\dot{\rho}_\phi + \delta\dot{\rho}_y \tag{28}$$
$$\delta\dot{\rho}_\phi = \frac{c}{2f_{T,0}T_I}\delta n_d \tag{29}$$
$$\delta\dot{\rho}_y = \frac{c}{2f_{T,0}T_I}\delta n_y \tag{30}$$

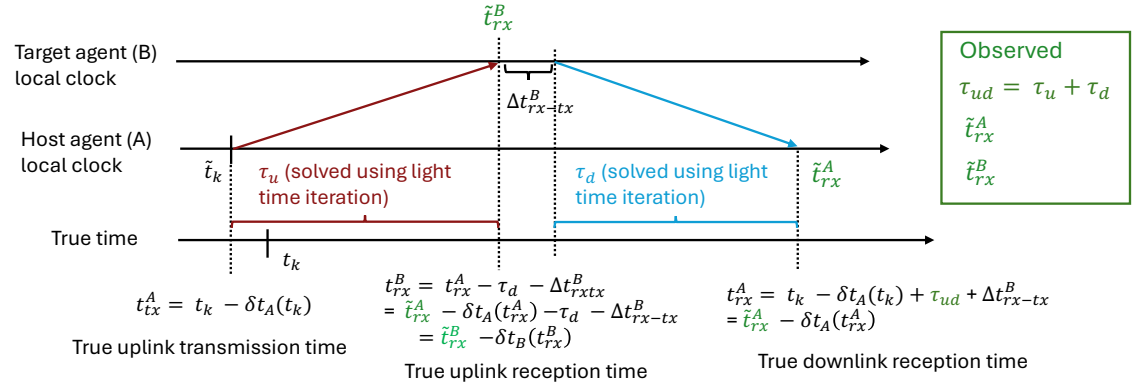

Figure 8: **Two-way ranging and time transfer measurement**

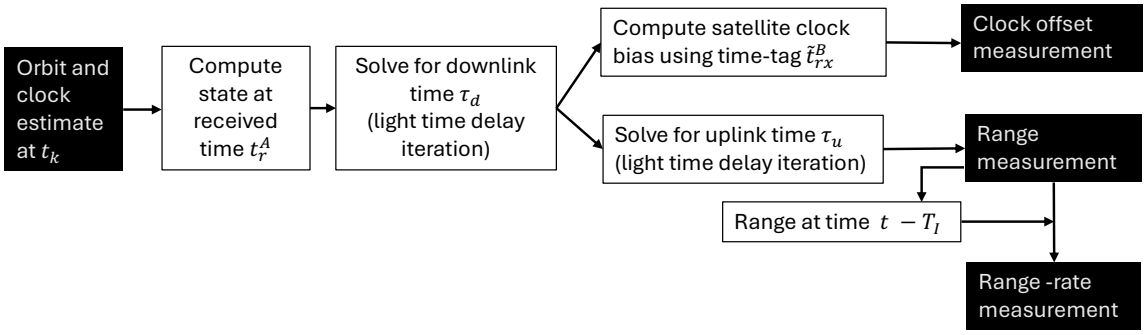

Figure 9: **Mapping between the states and the three two-way measurements**

Above, the phase noise $\delta\dot{\rho}_\phi$ is given as [14]

$$\begin{aligned}\delta n_d &\sim \mathcal{N}(0, \sigma^2_\phi)\\ \sigma_\phi &= \frac{\delta}{2\pi}\sqrt{\frac{B_L^{carrier} T_s(1+2\text{SNR})}{\text{SNR}^2}}\end{aligned} \tag{31}$$

where correction coefficient $\delta = 1.15$ for $BT_s = 0.25$ [14]. The oscillator frequency noise is given as

$$\begin{aligned}\delta n_y &\sim \mathcal{N}(0, \sigma^2_{\dot{\rho},y})\\ \sigma_{\dot{\rho},y} &= \frac{c\tau_{ud}}{2T_I}\sigma_y(T_I) \approx \frac{\rho_{ud}\sigma_y(1)}{T_I^{2/3}}\end{aligned} \tag{32}$$

where $\sigma_y(\tau)$ is the Allan deviation of the oscillator clock for duration τ. In summary, the measurement error is modeled as

$$\begin{aligned}\epsilon_{\dot{\rho}} &\sim \mathcal{N}(0, \sigma_{\dot{\rho}})\\ \sigma^2_{\dot{\rho}} &= \sigma^2_\phi + \sigma^2_{\dot{\rho},y}\end{aligned} \tag{33}$$

Two-way time transfer: Two-way time transfer measurement is obtained using the reception timestamp recorded at target agent B, $\tilde{t}^B_{rx}$, and the estimated downlink time τ_d. The following equality holds for the true uplink reception time t^B_{rx}:

$$\begin{aligned}t^B_{rx} &= t^A_{rx} - \tau_d - \Delta t^B_{rx-tx}\\ &= \tilde{t}^A_{rx} - \delta t_A(t^A_{rx}) - \tau_d - \Delta t^B_{rx-tx}\\ &= \tilde{t}^B_{rx} - \delta t_B(t^B_{rx})\end{aligned} \tag{34}$$

By moving the terms of the last two equations in (34) , we obtain the clock bias difference as follows

$$\begin{aligned}\delta^{AB}_t &= \tilde{t}^B_{rx} - (\tilde{t}^A_{rx} - \tau_d - \Delta t^B_{rx-tx})\\ &= \delta t^B(t^B_{rx}) - \delta t^A(t^A_{rx}) + \epsilon_t\end{aligned} \tag{35}$$

where δ^{AB}_t is the difference between the clock biases at agent A and B, and $\epsilon_t \sim \mathcal{N}(0, \sigma^2_t)$ is the time-tagging error of t^B_{rx}. We assumed that the σ_t are in the order of nanoseconds [17].

Note that the error of δ^{AB}_t also depends on the accuracy of estimating the downlink light-time delay τ_d, which depends on the orbit determination accuracy. Therefore, the orbit determination and time synchronization becomes a coupled problem.

One-way Measurement

For MSS-RGT links, we also consider a scenario where one-way downlink from transmitter B to receiver A is used instead of two-way links. Here, the transmitter is the RGT satellite and the receiver is the MSS. This approach would remove the need for the MSS to transmit the signals to (multiple) RGT orbiters, increasing the operational flexibility. In addition, if the RGT satellites are transmitting navigation signals to the surface, MSS can use these signals to obtain the pseudorange and pseudorange rate measurements, and the RGT satellites would not have to generate dedicated links for ODTS.

In the one-way link scenario, the following pseudorange

measurement is obtained instead of the range measurement

$$\begin{aligned}\rho_{BA,1} &= c\tau_d + \epsilon_{\rho,1} \\ &= \|\boldsymbol{r}^A(t_{rx}^A) - \boldsymbol{r}^B(t_{tx}^B)\| \\ &\quad + c\left[\delta t^B(t_{tx}^B) - \delta t^A(t_{rx}^A)\right] + \epsilon_{\rho,1} \\ t_{tx}^B &= t_{rx}^A - \tau_d\end{aligned} \tag{36}$$

As shown above, when the one-way range is used, the range and the clock bias difference are coupled. To solve for the light-time delay equation, we need the estimate of the transmitter clock bias $\delta t^B(t_{tx}^B)$.

The range-rate measurement is obtained by integrating the observed phase measurements,

$$\begin{aligned}\bar{\dot{\rho}}_{BA,1} &= \frac{c}{f_{T,0}T_I} n_d + \epsilon_{\dot{\rho},1} \\ &= \frac{1}{T_I}\left(\rho_{BA,1}(t) - \rho_{BA,1}(t - T_I)\right) + \epsilon_{\dot{\rho},1}\end{aligned} \tag{37}$$

We assumed that the errors $\epsilon_{\rho,1}$ and $\epsilon_{\dot{\rho},1}$ are sampled from Gaussian distribution, and its variance $\sigma_{\rho,1}^2, \sigma_{\dot{\rho},1}^2$ are given as follows [14]:

$$\sigma_{\rho,1} = T_c c L_{jitt} \sqrt{\frac{B_L^{chip} T_c}{\pi^2 L_{ck} \frac{P_T T_s}{N_0} 2 J_1^2(m_{RG})}} \tag{38}$$

$$\sigma_{\dot{\rho},1} = \frac{c}{f_{T,0}T_I}\left(\frac{c\tau_{ud}}{T_I}\sigma_y(T_I) + \frac{\delta}{2\pi}\sqrt{\frac{B_L^{carrier} T_s(1+2\text{SNR})}{\text{SNR}^2}}\right) \tag{39}$$

4. ORBIT DETERMINATION AND TIME SYNCHRONIZATION

State Formulation

Due to the coupling between the orbital states and the clock offset parameters explained in the previous section, we jointly estimate them in our filter. The state for satellite i is

$$x^{(i)} = \begin{bmatrix} r_x^{(i)} & r_y^{(i)} & r_z^{(i)} & v_x^{(i)} & v_y^{(i)} & v_z^{(i)} & \delta t^{(i)} & \delta\dot{t}^{(i)} \end{bmatrix} \tag{40}$$

where (r_x, r_y, r_z) and (v_x, v_y, v_z) are the position and velocity of the satellite at Mars centered inertial frame, respectively, and δt and $\delta\dot{t}$ is the clock bias and the clock drift of the onboard clock. The axes of the inertial frame is taken to be aligned with the J2000 frame.

The joint state to be estimated in the centralized batch filter is

$$x = \begin{bmatrix} x^{(1)} & x^{(2)} & x^{(3)} & x^{(4)} & x^{(5)} \end{bmatrix} \tag{41}$$

where $x^{(1)}, x^{(2)}, x^{(3)}, x^{(4)}, x^{(5)}$ are the states of satellite RGT1, RGT2, RGT3, AS1, AS2 in Table 4.

Orbit Dynamics

The orbit dynamics used for true state propagation and for time update in the filter are shown in Table.6. At the altitude for 1/2 RGT orbit and the areostationary orbit, the dominating perturbations other than the gravity terms is the solar radiation pressure (SRP) [18]. In the truth dynamics, the SRP acceleration $a_\odot \in \mathbb{R}^3$ is modeled using a cannonball model [11]:

$$\begin{aligned}a_\odot &= -C_R \frac{A^u \Phi_\odot}{cM^u}\left(\frac{(1\text{AU})}{d_\odot}\right)^2 \hat{e}_{Sun} \\ &= -\gamma_{srp}\frac{\Phi_\odot}{c}\left(\frac{(1\text{AU})}{d_\odot}\right)^2 \hat{e}_{Sun}\end{aligned} \tag{42}$$

where $\Phi_\odot$ denotes the solar flux at 1AU (=1360 W/m^2), A^u and M^u denote the surface area and mass of the Mars orbiter, respectively. Also, 1AU denotes 1 astronomical unit (=1.498×10^8 km), $d_\odot$ denotes the heliocentric distance to the Mars orbiter, $\hat{e}_{Sun}$ denotes the sun unit direction vector from the satellite, and $C_R = 1 + \epsilon$ denotes the coefficient of reflection, where $0 \le \epsilon \le 1$ is the radiation reflection ratio of the spacecraft body.

In the filter, we assumed that there exists a 10% bias in the estimated parameter C_R. In our future work, we plan to modify the filter so that we estimate the SRP ballistic coefficient γ_{srp} for each satellite with the other states.

Table 6: **Orbit Dynamics Model**

	Truth	**Filter**
Mars gravity	10×10	5×5
Third body gravity	Sun, Phobos Deimos	Sun, Phobos Deimos
Solar radiation pressure (SRP)	Cannonball $M_u = 1000$ kg $A_u = 20\ m^2$ $C_R = 1.5$	Cannonball $M_u = 1000$ kg $A_u = 20\ m^2$ $C_R = 1.35$
Unmodeled acceleration (σ_{acc})	None	$1 \times 10^{-8}\ m/s^2$

Clock Dynamics

The clock bias $\tau^u \in \mathbb{R}$ and the clock drift $\dot{\tau}^u \in \mathbb{R}$ are propagated using the following discrete, two-state error model taken from [19].

$$\begin{bmatrix}\delta t \\ \delta\dot{t}\end{bmatrix}_k = \Phi^{clk}(t_k, t_{k-1}) \begin{bmatrix}\delta t \\ \delta\dot{t}\end{bmatrix}_{k-1} + \boldsymbol{\epsilon}_k^{clk} \tag{43}$$

$$\Phi^{clk}(t_k, t_{k-1}) = \begin{bmatrix}1 & \Delta t \\ 0 & 1\end{bmatrix} \tag{44}$$

$$\epsilon_k^{clk} = \begin{bmatrix}\epsilon_\tau & \epsilon_{\dot{\tau}}\end{bmatrix}_k^\top \sim \mathcal{N}(0, Q_{clk}) \tag{45}$$

$$Q_{clk} = \begin{bmatrix}\sigma_1^2\Delta t + \frac{1}{3}\Delta t^3\sigma_2^2 & \frac{1}{2}\Delta t^2\sigma_2^2 \\ \frac{1}{2}\Delta t^2\sigma_2^2 & \Delta t\sigma_2^2\end{bmatrix} \in \mathbb{R}^{2\times 2} \tag{46}$$

$$\Delta t = t_k - t_{k-1} \tag{47}$$

where the noise vector $\epsilon_k^{clk} = \begin{bmatrix}\epsilon_\tau & \epsilon_{\dot{\tau}}\end{bmatrix}_k^\top$ is a Gaussian noise sampled from the random-walk process of the clock, and σ_1, σ_2 are the diffusion components of the clock phase deviation and the clock frequency deviation. For the onboard clock, we assumed the usage of Mini-RAFS [20], where its parameters are given as $\sigma_1 = 1 \times 10^{-11}$ and $\sigma_2 = 1 \times 10^{-15}$. These parameters are estimated from the Allan deviation plot in the data sheet using the method shown in [21].

Centralized Batch Filtering

The orbits and clock offsets of all satellites are jointly estimated in batches at the fusion center. The fusion center could be a surface station, one of the Martian satellites, or at DSN, depending on the configuration. After collecting all the measurements for time epoch $t_1, \ldots, t_N$, we run the iterative Extended Kalman Smoother (iEKS) [22] to estimate the states of all satellites.

The iEKS consists of two steps: the forward recursion and the backward recursion. The forward recursion is written as follows.

$$\hat{x}_{k-1}^{k} = f(\hat{x}_{k-1}^{k-1}, t_k, t_{k+1}) \tag{48}$$
$$\hat{P}_{k-1}^{k} = \Phi_{k,k-1}\hat{P}_{k-1}^{k-1}\Phi_{k,k-1}^{\top} + Q_k \tag{49}$$
$$\hat{x}_{k}^{k} = \hat{x}_{k-1}^{k} + K_k \Delta y_k \tag{50}$$
$$\Delta y_k = y_k - g(\hat{x}_{k-1}^{k}) \tag{51}$$
$$\hat{P}_{k}^{k} = J_k \hat{P}_{k-1}^{k} J_k^{\top} + K_k R_k K_k^{\top} \tag{52}$$
$$K_k = \hat{P}_{k-1}^{k} H_k^{\top} (H_k \hat{P}_{k-1}^{k} H_k^{\top} + R_k)^{-1} \tag{53}$$
$$J_k = I_n - K_k H_k \tag{54}$$
$$H_k = \left.\frac{\partial g(x)}{\partial x}\right|_{x=\hat{x}_{k-1}^{k}} \tag{55}$$
$$\Phi_{k,k-1} = \left.\frac{\partial f(x, t_k, t_{k+1})}{\partial x}\right|_{x=\hat{x}_{k-1}^{k}} \tag{56}$$

where $\hat{x}_l^m, \hat{P}_l^m$ denotes the estimate of x and its covariance at timestep m based on measurements at timestep $1, \ldots, l$, respectively. Function $x_{k+1} = f(x_k, t_k, t_{k+1})$ and $y_k = g(x_k)$ are the functions that propagate the state to the next timestep, and the function that maps the state to measurements, respectively. The measurement function Jacobian H_k and the state transition matrix $\Phi_{k,k-1}$ are computed using automatic differentiation [23].

Q_k is the process noise, which is constructed as follows in our filter.

$$Q_k = \begin{bmatrix} Q_{rvc} & 0_{8\times8} & 0_{8\times8} & 0_{8\times8} & 0_{8\times8} \\ 0_{8\times8} & Q_{rvc} & 0_{8\times8} & 0_{8\times8} & 0_{8\times8} \\ 0_{8\times8} & 0_{8\times8} & Q_{rvc} & 0_{8\times8} & 0_{8\times8} \\ 0_{8\times8} & 0_{8\times8} & 0_{8\times8} & Q_{rvc} & 0_{8\times8} \\ 0_{8\times8} & 0_{8\times8} & 0_{8\times8} & 0_{8\times8} & Q_{rvc} \end{bmatrix} \in \mathbb{R}^{40\times40} \tag{57}$$

$$Q_{rvc} = \begin{bmatrix} Q_{rv} & 0_{6\times2} \\ 0_{2\times6} & Q_{clk} \end{bmatrix} \in \mathbb{R}^{8\times8} \tag{58}$$

$$Q_{rv} = \begin{bmatrix} \frac{1}{3}\Delta t^3 Q^a & \frac{1}{2}\Delta t^2 Q^a \\ \frac{1}{2}\Delta t^2 Q^a & \Delta t Q^a \end{bmatrix} \in \mathbb{R}^{6\times6} \tag{59}$$

$$Q_a = \sigma_a^2 I_3 \tag{60}$$

where $Q^a \in \mathbb{R}^{3\times3}$ is the covaraince of the unmodeled acceleration σ_a [22, 24].

R_k is the measurement noise matrix, which is a diagonal matrix where its diagonal elements are the stacked vector of squared measurement noises for all $m_{k,1}+m_{k,2}$ links at time epoch t_k, where $m_{k,2}$ is the number of two-way links and $m_{k,1}$ is the number of one-way links.

$$R_k = \text{diag}(\sigma_1^{(2)}, \ldots, \sigma_{m_{k,1}}^2) \in \mathbb{R}^{m_k \times m_k} \tag{61}$$
$$m_k = 3m_{k,2} + 2m_{k,1} \tag{62}$$

After the forward recursion reaches the final timestep, we run the following backward recursion for $k = N-1, \cdots, 1$:

$$\hat{x}_N^k = \hat{x}_k^k + S_k(\hat{x}_N^{k+1} - \hat{x}_k^{k+1}) \tag{63}$$
$$\hat{P}_N^k = \hat{P}_k^k + S_k \hat{P}_N^{k+1} S_k^{\top} \tag{64}$$
$$S_k = \hat{P}_k^k \Phi_{k+1,k}^{\top} (\hat{P}_k^{k+1})^{-1} \tag{65}$$

where N is the total number of timesteps.

We repeat the forward recursion and the backward recursion until convergence. Convergence is judged based on the relative RMS residual error ΔRMS_i compared to the previous iteration [22]

$$\begin{aligned} \Delta RMS_i &= \frac{RMS_i}{\|RMS_i - RMS_{i-1}\|} \\ RMS_i &= \sum_{k=1}^{T} \frac{\Delta y_k^T \Delta y_k}{\text{diag}(R_k)} \end{aligned} \tag{66}$$

where i is the iteration index, k is the time index, Δy_k is the measurement residual defined in Eq (51), and R_k is the measurement noise matrix. When the threshold is $\Delta RMS_i < 0.001$, it takes around 5-10 iterations until convergence.

5. ODTS SIMULATION

Simulation Configurations

The simulation parameters used are listed in Table.7. Note that the transmitter and receiver parameters are given in Table 5, and the dynamics model is shown in Table 6 in the previous sections.

We test different combinations of links, to evaluate their effect on the overall ODTS performance.

ISL Only. This configuration only utilizes the inter-satellite link between the satellites for ODTS. For the purpose of communication payload sizing, we assumed the ISL between the RGT orbiters and the AS orbiters is active only when the inter-satellite ranges are below 22500 km, which roughly corresponds to the maximum range between the two RGT orbiters. We assumed AS-AS and RGT-RGT links are continuously available. The visibility of the link is shown in Figure 10a. All satellite clocks are synchronized to the AS2 satellite in this configuration.

ISL + DSN-AS. In this configuration, we combine ISL and two-way range and range-rate measurements of the two AS orbiters from the DSN. The AS orbiters are assumed to have larger antennas for communication with Earth. We set an elevation mask of 10 degrees and account for the occultation from Mars. The visibility of the links for the three measurement types is shown in Figure 10b. At the initial simulation epoch we used (2035/03/01 00:00:00 Barycentric Dynamic Time), there is a 75 minutes occultation due to Mars blockage. By using, all 3 DSN stations whenever they are

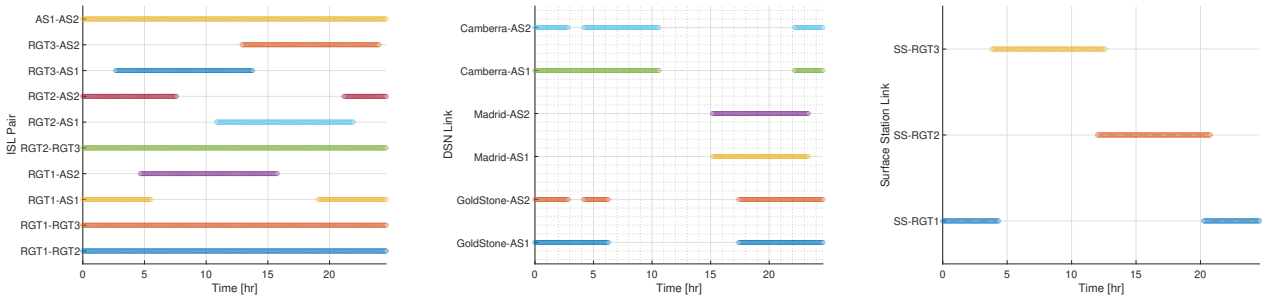

(a) Intersatellite link (b) DSN-AS link (c) MSS-RGT link

Figure 10: **Visibility of the three types of links over one Mars sidereal day**

Table 7: **Parameters Used for ODTS Simulation**

Parameters	Value
Simulation epoch	2035/03/01 00:00:00
Simulation length	24.6 hours
Measurement interval	60 sec
Elevation mask (DSN)	10°
Elevation mask (MSS)	10°
(Lat, Lon) of MSS	(0°, 0°)
DSN range error	1m (1-σ)
DSN range rate error	0.1mm/s (1-σ)
Time-tagging error (σ_t)	3 ns (1-σ)
DSN Doppler integration Time	60 s
ISL Doppler integration Time	1 s
Initial position error	1000 m (1-σ)
Initial velocity error	1 mm/s (1-σ)
Initial clock bias error	1 μ s (1-σ)
Initial clock drift error	1 ns/s (1-σ)
Data rate (MSS-RGT)	50 Mbps
Data rate (ISL)	10 Mbps

available, AS1 and AS2 can have a link with DSN for 81.7% and 76.6% of a sidereal day, respectively. All satellite clocks are synchronized to the AS2 satellite in this configuration. Also, for the DSN links we did not assume using GMSK+PN links, and used the parameters shown in Table 7 to compute the range, range-rate, and time-tagging errors.

ISL + MSS-RGT (2-way). In this configuration, we combine ISL and two-way range and range-rate measurements of the three RGT orbiters from the MSS. The longitude and latitude of the MSS is fixed at 0°, and we assume its position is perfectly known. The visibility of the link is shown in Figure 10c.

ISL + MSS-RGT (1-way). In this configuration, we combine ISL and one-way range and range-rate measurements from the three RGT orbiters to the MSS.

For each of these configurations, we evaluate the performance based on 30 Monte-Carlo runs. At each Monte-Carlo run the initial state estimation error is sampled differently from a normal distribution, where variances are shown in Table 7.

Centralized Batch Filtering

In centralized batch filtering, all measurements over the entire sidereal day (24.6 hours) are downlinked to MSS (ISL + MSS) or DSN (ISL + DSN) or areostationary satellite (ISL-only case) and processed in batch. In this paper, we assume instantaneous data transfer of PNT observables and states to and from the fusion location. Additionally, we do not analyze the growth of orbit and clock estimate errors between state estimate updates at these fusion centers. As a result, this study provides a lower bound on the orbit and time estimation error that each satellite would be able to access.

The estimation errors on the centralized batch filtering are shown in Table 8. For all configurations, the radial direction position is estimated in sub-meter level accuracy, and the clock bias is synchronized in sub-nanosecond level accuracy. The best estimation accuracy is achieved when using the ISL + MSS configuration. Since all satellites are located in circular and nearly equatorial orbit, when only the ISL is used, the ambiguity of the tangential direction and the normal direction cannot be resolved because of the symmetrical ambiguity of the relative geometry, as shown in Figure 11. Since the RGT and AS orbits are in high altitudes, we cannot utilize the higher order gravity terms to resolve this ambiguity [25]. Therefore, in this weakly observable setting, we need an anchor whose absolute position is well-known to fix this ambiguity.

Adding a DSN measurement anchors one of the absolute positions of the satellites, and resolves this tangential ambiguity, but a large estimation error remains in the normal direction because the line-of-sight vectors to Earth are only slightly off the orbital planes of the satellites, as shown in Figure 12. Note that the values obtained in this study do not indicate the maximum ODTS accuracy that could be achieved by DSN measurements. A better orbit determination accuracy could potentially be obtained by using longer arcs for orbit determination, using a higher fidelity dynamics model for the filter, and using advanced ODTS methods such as Delta-DOR [26].

Using the surface station on Mars resolves both the tangential and normal ambiguity. Since the MSS is much closer to the orbiters compared to DSN, the MSS-RGT link has much more geometrical diversity than the DSN link, which helps resolve the normal ambiguity. Lower ODTS error is achieved by using a two-way link for the surface links instead of one-way links, since the orbit states and the clock biases are more decoupled in the two-way measurements compared to one-way pseudorange and pseudorange rates.

Table 8: **Mean position and velocity estimation error of the batch filter over a sidereal day. The displayed values are the root-mean-squared errors over 30 Monte-Carlo runs. For ISL only and the ISL + DSN case, the estimated clock biases are the relative clock bias with respect to AS2. When only the ISL is used, the ambiguity of the tangential direction and the normal direction could not be resolved because of the symmetrical ambiguity of the relative geometry. Adding a DSN measurement resolves this tangential ambiguity, but a large estimation error remains in the normal direction because the line-of-sight vectors to Earth are only slightly off the orbital planes of the satellites. Using the surface station on Mars resolves both the tangential and normal ambiguity. Sub-meter-level accuracy is achieved with two-way links for surface links, while meter-level accuracy is achieved with one-way surface links.**

Measurements	Sat	Position				Velocity				Clock
		3D [m]	Radial [m]	Tangential [m]	Normal [m]	3D [mm/s]	Radial [mm/s]	Tangential [mm/s]	Normal [mm/s]	Bias [ns]
ISL 2-way	RGT1	1664.5	0.17	1125.0	1226.7	236.0	0.031	0.033	173.8	0.68
	RGT2	1678.4	0.20	1168.3	1205.0	238.2	0.029	0.045	171.1	0.66
	RGT3	1677.9	0.21	1165.6	1206.9	238.0	0.030	0.047	171.2	0.66
	AS1	2664.6	0.26	1850.7	1917.0	188.8	0.028	0.027	135.8	0.63
	AS2	2663.7	0.33	1850.6	1915.9	188.9	0.027	0.026	135.9	-
	Total	2126.0	0.24	1472.4	1533.6	219.3	0.029	0.037	158.6	0.66
ISL 2-way + DSN 2-way	RGT1	18.03	0.06	3.41	17.71	2.56	0.014	0.011	2.51	0.41
	RGT2	18.44	0.05	6.10	17.40	2.61	0.012	0.014	2.47	0.41
	RGT3	18.19	0.04	1.76	18.10	2.58	0.010	0.017	2.57	0.40
	AS1	28.50	0.06	2.78	28.36	2.02	0.012	0.010	2.01	0.34
	AS2	28.60	0.07	2.82	28.46	2.03	0.012	0.009	2.02	0.00
	Total	22.92	0.06	3.68	22.62	2.37	0.012	0.012	2.33	0.39
ISL 2-way + MSS 2-way	RGT1	0.328	0.024	0.089	0.315	0.045	0.005	0.010	0.042	0.34
	RGT2	0.398	0.032	0.146	0.369	0.056	0.005	0.007	0.051	0.34
	RGT3	0.447	0.029	0.116	0.430	0.063	0.006	0.007	0.060	0.33
	AS1	0.486	0.018	0.109	0.474	0.033	0.004	0.006	0.031	0.37
	AS2	0.474	0.031	0.189	0.434	0.033	0.005	0.008	0.028	0.37
	Total	0.431	0.027	0.134	0.408	0.047	0.005	0.008	0.044	0.35
ISL 2-way + MSS 1-way	RGT1	1.42	0.07	0.26	1.39	0.200	0.017	0.014	0.197	0.33
	RGT2	1.41	0.06	0.17	1.40	0.200	0.013	0.016	0.198	0.32
	RGT3	1.42	0.05	0.14	1.41	0.202	0.013	0.018	0.200	0.30
	AS1	2.18	0.07	0.20	2.17	0.154	0.015	0.010	0.153	0.36
	AS2	2.19	0.08	0.21	2.18	0.154	0.014	0.010	0.153	0.37
	Total	1.77	0.07	0.20	1.75	0.184	0.015	0.014	0.182	0.34

Note that the timing accuracy is maintained in a similar ballpark irrespective of the method and the orbit determination accuracy. This indicates avenues for further compute and algorithmic efficiency in future work in decoupling the timing estimation from orbit estimation or reducing cadence for timing estimation.

6. Conclusion

To enable future human exploration on Mars, it is necessary to develop a dedicated network of satellites that provide both communication relay and positioning, navigation, and timing (PNT) service in Mars' orbit and on its surface.

In this work, we first addressed the design of the next-generation Mars constellation with a focus on the following three objectives: coverage between ±30° latitude, communication data volume, and surface user PNT performance. By analyzing the trade-off space, we proposed a notional constellation comprising five satellites: two orbiters at areostationary orbit and three orbiters in an inclined ½ repeating ground track orbit, which balances the three objectives effectively.

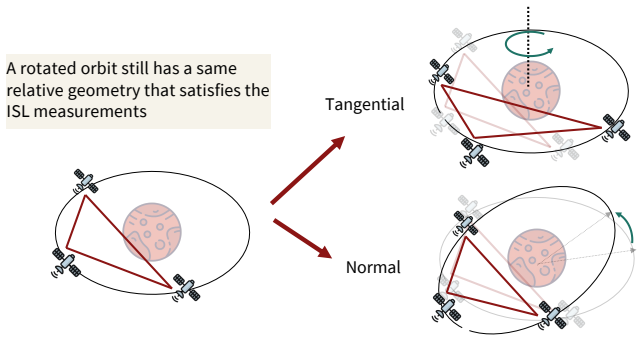

Figure 11: **The rotational ambiguity when using only ISL measurements between satellites at the same plane in circular orbit.**

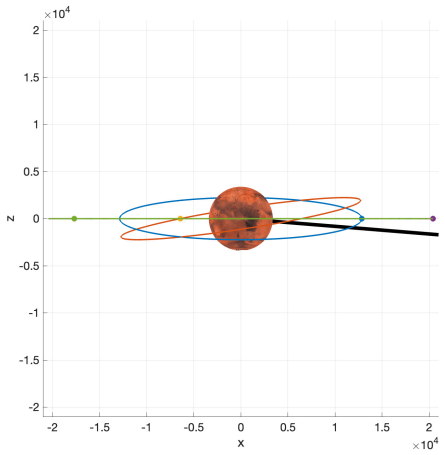

Figure 12: The direction of the DSN (black line) in inertial frame aligned with Mars body axis (at initial time epoch). The green and purple line (marker) shows the areostationary orbits (initial position), and the red, blue, yellow line (marker) shows the RGT orbits (initial position)

In the second part of the paper, we proposed an ODTS framework for the MRN orbiters that integrates three different methodologies: DSN tracking, ISLs, and links with a Mars surface station (MSS). The proposed framework estimates the orbit and clock biases of all satellites at a fusion center in batches. Through Monte Carlo simulations, we show that we are not able to resolve the tangential and normal direction ambiguity, if only ISL was used. By using the MSS to act as an anchor node, we could resolve this ambiguity, and the orbit determination error is reduced significantly, achieving a sub-meter-level orbit determination error for the 2-way surface-link case and meter-level orbit determination error for the 1-way surface-link case.

Future work will focus on increasing the fidelity of the simulation by modeling relativistic effects, errors in frame conversions, and uncertainty in MSS location knowledge. We also plan to extend the framework to perform ephemeris fitting and predict future orbits. Finally, we plan to investigate a distributed ODTS framework to update the orbits and time more frequently, and to reduce the communication burden to downlink all measurements to the fusion center.

ACKNOWLEDGMENTS

A portion of this research was carried out at the Jet Propulsion Laboratory, California Institute of Technology, under a contract with the National Aeronautics and Space Administration (80NM0018D0004).

REFERENCES

[1] R. Gladden, E. Pereira, and B. Sauer, "Lessons learned from the mars relay network: Considerations for future relay networks," in *2024 IEEE Aerospace Conference*, 2024, pp. 1–16.

[2] D. D. Wenkert, R. E. Gladden, C. D. Edwards, P. Schmitz, M. Denis, and A. J. Winton, *Enabling International Data Relay at Mars*. Cham: Springer International Publishing, 2017, pp. 175–205. [Online]. Available: https://doi.org/10.1007/978-3-319-51941-8_8

[3] J. Choi, R. Verma, and S. Malhotra, *Achieving Fast Operational Intelligence in NASA's Deep Space Network Through Complex Event Processing*, 2016. [Online]. Available: https://arc.aiaa.org/doi/abs/10.2514/6.2016-2375

[4] R. E. Gladden, C. H. Lee, C. D. Edwards, M. A. Viotti, and R. M. Davis, "A dedicated relay network to enable the future of mars exploration," in *2021 IEEE Aerospace Conference (50100)*, 2021, pp. 1–14.

[5] Y. N. Long, C. H. Lee, and R. Gladden, "On the orbit constellation assessment for the next-generation mars telecommunications orbiters," in *2023 IEEE Aerospace Conference*, 2023, pp. 1–10.

[6] P. W. Kelly and R. Bevilacqua, "Constellation design for mars navigation using small satellites," in *2018 AIAA Aerospace Sciences Meeting*, 2018. [Online]. Available: https://arc.aiaa.org/doi/abs/10.2514/6.2018-1538

[7] S. Molli, D. Durante, G. Boscagli, G. Cascioli, P. Racioppa, E. Alessi, S. Simonetti, L. Vigna, and L. Iess, "Design and performance of a martian autonomous navigation system based on a smallsat constellation," *Acta Astronautica*, vol. 203, pp. 112–124, 2023. [Online]. Available: https://www.sciencedirect.com/science/article/pii/S0094576522006488

[8] P. Romero, B. Pablos, and G. Barderas, "Analysis of orbit determination from earth-based tracking for relay satellites in a perturbed areostationary orbit," *Acta Astronautica*, vol. 136, pp. 434–442, 2017. [Online]. Available: https://www.sciencedirect.com/science/article/pii/S0094576516312188

[9] "Simultaneous Transmission of GMSK Telemetry and PN Ranging," Tech. Rep. CCSDS 413.1-G-2, 2021.

[10] "The future mars communication architecture," *Interagency Operations Advisory Group Mars and Beyond Communications Architecture Working Group*, vol. 1, 2022.

[11] O. Montenbruck and E. Gill, *Satellite Orbits: Models, Methods and Applications*. Springer Berlin Heidelberg, 2000.

[12] E. Kaplan and C. Hegarty, *Understanding GPS/GNSS: Principles and Applications, Third Edition*. Artech, 2017.

[13] G. P. Calzolari, E. Vassallo, G. Sessler, and M. Visintin, "Gmsk/pn for high rate telemetry and high accuracy ranging of lagrange and mars missions," *SpaceOps 2014 Conference*, 2014. [Online]. Available: https://arc.aiaa.org/doi/abs/10.2514/6.2014-1851

[14] "Simultaneous transmission of gmsk telemetry and pn ranging," *CCSDS Informational Report, 413.1-G-2*, 2021.

[15] M. Abramowitz, *Handbook of Mathematical Functions, With Formulas, Graphs, and Mathematical Tables,*. USA: Dover Publications, Inc., 1974.

[16] P. Grenfell, "Systems performance analysis for autonomous spacecraft navigation within satellite constellations using intersatellite optical communications links," Ph.D. dissertation, MASSACHUSETTS INSTITUTE OF TECHNOLOGY, 2024.

[17] K. Andrews, J. Hamkins, S. Shambayati, and V. Vil-

nrotter, "Telemetry-based ranging," in *2010 IEEE Aerospace Conference*, 2010, pp. 1–16.

[18] I. Suchantke, F. Letizia, V. Braun, and H. Krag, "Space sustainability in martian orbits — first insights in a technical and regulatory analysis," *Journal of Space Safety Engineering*, vol. 7, no. 3, pp. 439–446, 2020, space Debris: The State of Art. [Online]. Available: https://www.sciencedirect.com/science/article/pii/S2468896720300677

[19] L. Galleani, "A tutorial on the two-state model of the atomic clock noise," *Metrologia*, vol. 45, no. 6, p. S175, 2008.

[20] Orolia, "ispace+^{TM} minirafs spec," 2021. [Online]. Available: https://www.orolia.com/wp-content/uploads/2021/07/Spectratime-miniRAFS-Spec-01-19-21-1.pdf

[21] C. Zucca and P. Tavella, "The clock model and its relationship with the allan and related variances," *IEEE Transactions on Ultrasonics, Ferroelectrics, and Frequency Control*, vol. 52, no. 2, pp. 289–296, 2005.

[22] B. D. Tapley, B. E. Schutz, and G. H. Born, *Statistical Orbit Determination*. Elsevier, 2004.

[23] A. G. Baydin, B. A. Pearlmutter, A. A. Radul, and J. M. Siskind, "Automatic differentiation in machine learning: a survey," 2018. [Online]. Available: https://arxiv.org/abs/1502.05767

[24] A. Myers, Kenneth, "Filtering theory methods and applications to the orbit determination problem for near-earth satellites," Ph.D. dissertation, The University of Texas at Austin, 1974.

[25] Z. Li, Y. Wang, and W. Zheng, "Observability analysis of autonomous navigation using inter-satellite range: An orbital dynamics perspective," *Acta Astronautica*, vol. 170, pp. 577–585, 2020. [Online]. Available: https://www.sciencedirect.com/science/article/pii/S0094576520300850

[26] D. W. Curkendall and J. S. Border, "Delta-dor: The one-nanoradian navigation measurement system of the deep space network—history, architecture, and componentry," *The Interplanetary Network Progress Report*, vol. 42, p. 193, 2013.

BIOGRAPHY

Keidai Iiyama *is a Ph.D. candidate in the Department of Aeronautics and Astronautics at Stanford University. He received his M.E. degree in Aerospace Engineering in 2021 from the University of Tokyo, where he also received his B.E. in 2019. His research is on positioning, navigation, and timing of lunar spacecraft and rovers, and system designs for lunar and Martian navigation systems.*

Sriramya Bhamidipati *received her M.S. and Ph.D. in Aerospace Engineering at the University of Illinois, Urbana-Champaign in 2017 and 2021, respectively. She obtained her B.Tech. in Aerospace from the Indian Institute of Technology, Bombay in 2015. She is currently a robotics technologist in the autonomous systems division at NASA JPL. Her research interests include sensor fusion, GPS, computer vision, lunar navigation, and space robotics. Before joining JPL, she worked as a postdoctoral scholar in the navigation and autonomous vehicles lab at Stanford University. She received the Amelia Earhart Fellowship in 2020 and was awarded best presentation at ION GNSS+ four times in 2016, 2017, 2021 and 2022.*

William W.Jun *received his B.S., M.S., and Ph.D. degrees in aerospace engineering from the Georgia Institute of Technology in Atlanta, Georgia in 2018, 2020, and 2023 respectively. He is currently a Telecommunications Engineer at NASA Jet Propulsion Laboratory (JPL). During his stay at Georgia Tech, he worked in the Space Systems Design Laboratory (SSDL) on various CubeSat missions as subsystem leads and as the Project Manager of Prox-1. He was a Research Fellow at NASA JPL in the summers of 2018 to 2023. His research interests include navigation architectures, navigation methods, and estimation techniques. He was a recipient of the NASA Space Technology Research Fellowship in 2019 and the M. Charles Fogg Best Paper Award at the 2024 IEEE Aerospace Conference.*

Grace Gao *is an assistant professor in the Department of Aeronautics and Astronautics at Stanford University. Before joining Stanford University, she was an assistant professor at University of Illinois at Urbana-Champaign. She obtained her Ph.D. degree at Stanford University. Her research is on robust and secure positioning, navigation, and timing with applications to manned and unmanned aerial vehicles, autonomous driving cars, as well as space robotics.*

Kar-Ming Cheung *received the B.S.E.E. degree from the University of Michigan, Ann Arbor, in 1984, and the M.S. and Ph.D. degrees from California Institute of Technology in 1985 and 1987, respectively. He is a Principal Engineer and Technical Group Supervisor in the Communication Architectures and Research Section (332) at JPL. His group supports design and specification of future deep-space and near-Earth communication systems and architectures. Since 1987, he has been with JPL where he is involved in research, development, production, operation, and management of advanced channel coding, source coding, synchronization, image restoration, and communication analysis schemes. Dr. Cheung received NASA's Exceptional Service Medal for his work on Galileo's onboard image compression scheme.*